Dynamic Architecture of Mycobacterial Outer Membranes Revealed by All-Atom Simulations

Turner P. Brown[1], Matthieu Chavent[2]*, and Wonpil Im[1,3]*

[1]Department of Bioengineering, Lehigh University, Pennsylvania 18015, USA

[2]Institut de Pharmacologie et Biologie Structurale, CNRS, Université de Toulouse, 205 route de Narbonne, 31400, Toulouse, France

[3]Department of Biological Sciences, Pennsylvania 18015, USA

*Corresponding authors: matthieu.chavent@ipbs.fr and wonpil@lehigh.edu

Abstract:

Tuberculosis remains a global health crisis due to the resilience of *Mycobacterium tuberculosis* (*Mtb*), largely attributed to its unique cell envelope. The impermeability and structural complexity of the outer membrane of this envelope, driven by mycolic acids and glycolipids, pose significant challenges for therapeutic intervention. Here, we present the first all-atom models of an *Mtb* outer membrane using molecular dynamics simulations. We demonstrate that α-mycolic acids adopt extended conformations to stabilize bilayers, with a phase transition near 338 K that underscores their thermal resilience. Lipids in the outer leaflet such as PDIM and PAT induce membrane heterogeneity, migrating to the interleaflet space and reducing lipid order. The simulated mycobacterial outer membrane has ordered inner leaflets and disordered outer leaflets, which contrasts with the outer membrane of Gram-negative bacteria. These findings reveal that PDIM- and PAT-driven lipid redistribution, reduced lipid order, and asymmetric fluidity gradients enable *Mtb's* outer membrane to resist host-derived stresses and limit antibiotic penetration, thereby promoting bacterial survival. Our work provides a foundational framework for targeting the mycobacterial outer membrane in future drug development.

Teaser:

Molecular dynamics simulations reveal the unique architecture of the mycobacterial outer membrane: a fluid outer leaflet and an ordered, tightly packed inner leaflet.

Introduction:

Tuberculosis (TB) has been known to humankind since ancient times. Commonly known as Phthisis in ancient Greece and Consumption in the 1800s, TB has a storied history, influencing cultures around the world and being notoriously difficult to treat. Despite increasing investments into detection and treatment development, an estimated 1.25 million people died of TB in 2023. This makes it the world's deadliest infectious disease, surpassing COVID-19 ("Global Tuberculosis Report 2024," n.d.). *Mycobacterium tuberculosis* (*Mtb*), the etiologic agent of TB, was first discovered in 1882 by Dr. Robert Koch. TB is a disease with a wide spectrum of manifestations – some individuals have active uncontrolled disease when the bacteria are actively replicating, whereas others may have controlled or latent infection when the bacteria may lie dormant intracellular in macrophages or other cells. *Mtb* is a slow-growing bacterium with a formidable cell wall characterized by acid fastness. Antibiotics targeting the cell wall (Isoniazid, Pretomanid) are prominent in multi-drug regimens for drug-susceptible and drug-resistant strains. However, these regimens take many months, and drug-resistant *Mtb* strains are an increasing problem, necessitating further drug development (Dartois and Dick, 2024).

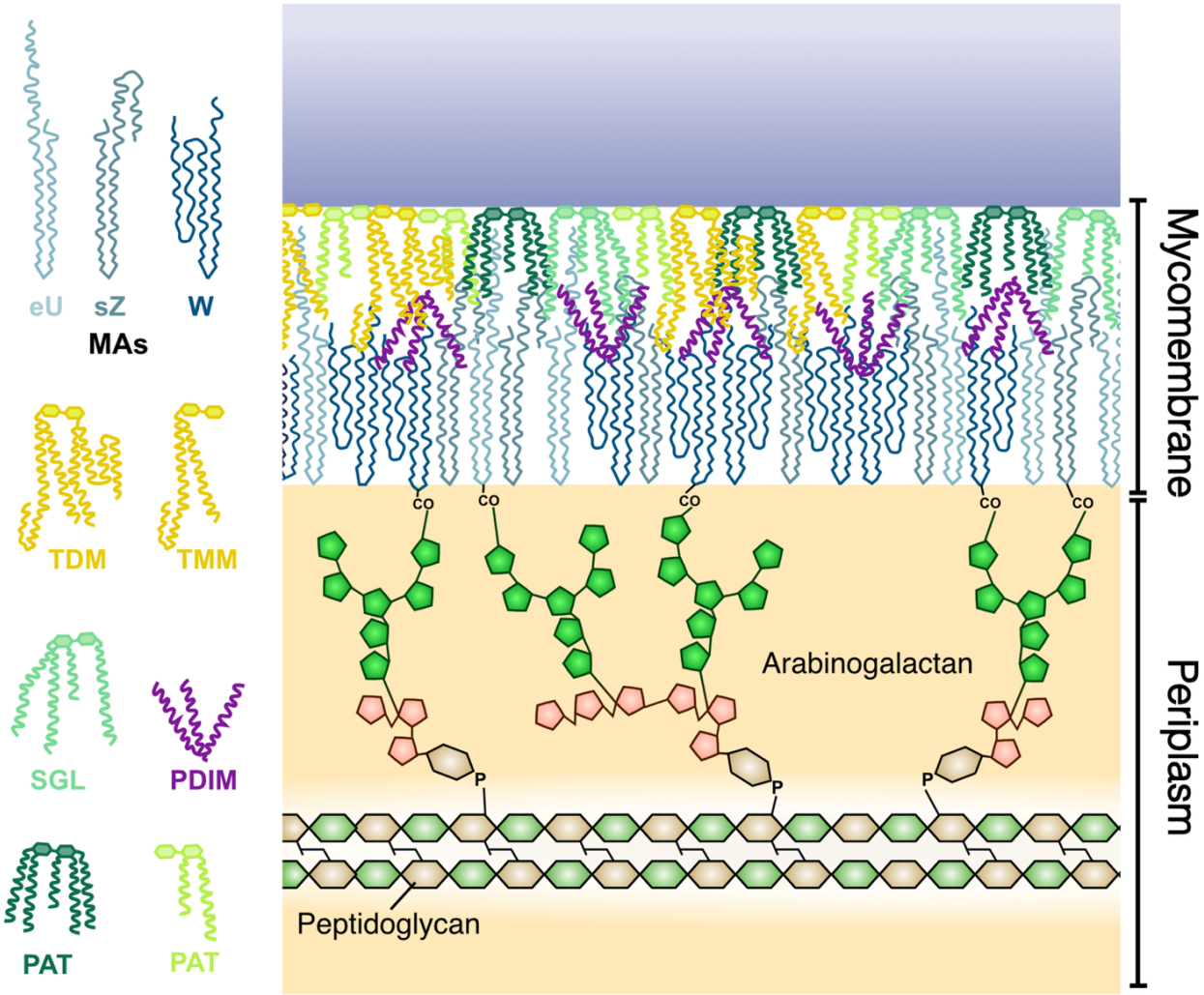

Figure 1. Schematic of a mycobacterial outer membrane composed of mycolic acids (MAs), trehalose di- and mono-mycolate (TDM and TMM), phthiocerol dimycocerosate (PDIM), sulphoglycolipids (SGL), and pentacyl and diacyl trehalose (PAT and DAT). This membrane is covalently attached to the peptidoglycan via the arabinogalactan.

The cell envelope of *Mtb* is unusually thick and impermeable. The innermost layer is a plasma membrane consisting of various phosphatidyl-*myo*-inositol mannosides (PIMs) and lipomannan. Just above the plasma membrane is a peptidoglycan layer bound to a layer of arabinogalactan (**Fig. 1**). Arabinogalactan sugars are covalently linked to mycolic acids in the inner leaflet of the mycobacterial outer membrane (MOM), also known as the mycomembrane. This is the bacterium's first defensive layer against external threats. The MOM is an asymmetric bilayer and the most complex layer of the cell envelope. Although its composition was unknown for decades, advancements in biochemical assays have yielded a reliable description of the native mycomembrane (Chiaradia et al., 2017). Lipoarabinomannan is also present in cell envelope, but its exact location is up for debate. Many models show it anchored in the inner membrane, but it has been shown to be surface-exposed, suggesting that it extends through the periplasm space and the outer membrane (Mishra et al., 2011; Torrelles and Chatterjee, 2023).

The mycomembrane inner leaflet is composed of ultra-long-chain fatty acids known as mycolic acids (MAs). MAs, which contain between 60 and 90 carbon atoms, consist of a long β-hydroxy chain and a short α-alkyl side chain (**Fig. 2A**). Further classification of MAs is based on functional groups, categorizing them into three groups: alpha, methoxy, and keto-MA. α-MAs contain cyclopropane groups at two positions along the β-hydroxy chain (proximal and distal); methoxy-MAs contain a methoxy group in the distal position; and keto-MAs contain a carbonyl group at the distal position (Marrakchi et al., 2014). These three MAs exist in varying concentrations depending on the species, and were shown to have distinct effects on monolayer and bilayer characteristics (Hasegawa and Leblanc, 2003; Kumar et al., 2025). α-MAs are of particular interest not only because of their extreme length, but also the presence of cyclopropane rings (**Fig. 2A**). Such ultra-long-chain fatty acids are able to adopt various folding patterns, which helps to regulate bilayer order and symmetry (Kawaguchi et al., 2022). Cyclopropanation of acyl chains tends to promote bilayer fluidity by interfering with lipid packing, enhancing the formation of *gauche* defects and increasing lipid diffusion. Based on bilayer simulations, Poger et al. showed that fatty acid cyclopropanation increases fluidity in the plasma membrane. Additionally, they found that *cis*- and *trans*-cyclopropane fatty acids have distinct ordering effects (Poger and Mark, 2015). In the case of MAs, the first observation of distinct folding patterns was made by Takeshi Hasegawa in 2004 using surface-enhanced Raman scattering (Hasegawa, 2004). Later studies described three major folding patterns in MAs (Groenewald et al., 2019, 2014; Savintseva et al., 2023): W, a fully folded shape in which the long chain folds in on itself twice (four parallel chains); Z, a semi-folded shape in which the long chain folds in on itself once (three parallel chains); and U, a fully extended shape in which the long chain does not fold in on itself (two parallel chains) (**Fig. 2B-D**). Although these conformations were observed in experimental and computational studies, they do not represent the complete diversity of folds that MAs can exhibit. In this study, we have analyzed the folding behavior and effects on bilayer stability of α-MAs in a

mycomembrane-like environment. We have also used the equilibrated symmetric bilayers to estimate reasonable areas per lipid and facilitate the modeling of stable asymmetric systems.

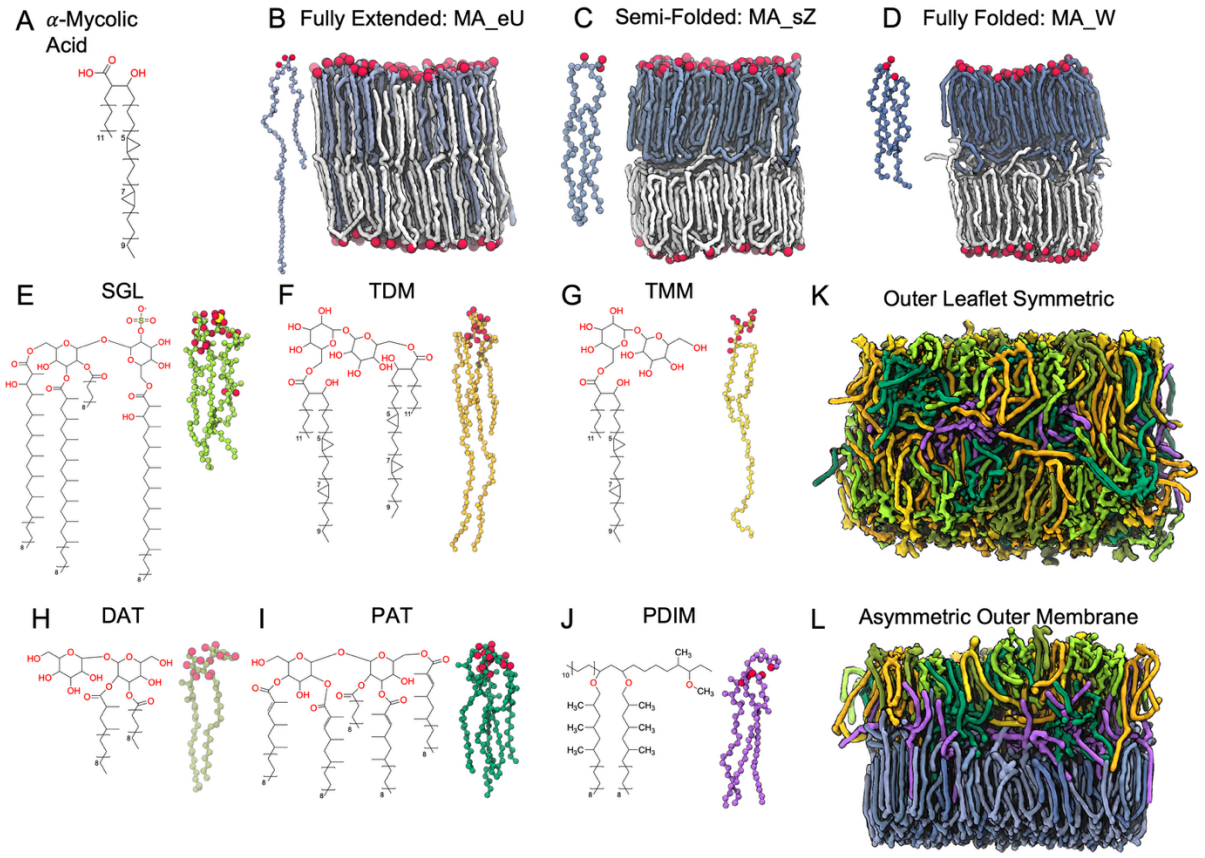

Figure 2. Chemical structures of mycobacterial lipids and membranes snapshots. A. Chemical structure of α-mycolic acid (α-MA) with 78 carbons. **B-D**. Initial three-dimensional (3D) conformations (left) and snapshots after 3 μs production of pure mycolic acid bilayers (right) with fully extended (MA_eU), semi-folded (MA_eZ), and fully folded (MA_W) conformations. Lipids in the upper leaflet are colored in light, medium, and dark blue, and lipids in the lower leaflet are colored in white. Oxygen atoms are shown as van der Waals spheres. **E-J**. Chemical structures (left) and initial conformations (right) of the six outer leaflet lipids. **K**. Snapshot after 3 μs production of the symmetric system containing outer leaflet lipids at 313 K (All_Lipids_313). **L**. Snapshot after 3 μs production of the whole mycobacterial outer membrane with asymmetry of lipids at 313 K (Asym_313 system). Lipid colors in **K** and **L** match the colors of the initial 3D conformations.

The outer leaflet of the mycomembrane contains many structurally and functionally diverse glycolipids, which aid in pathogenicity and virulence of *Mtb*. Phthiocerol dimycocerosate (PDIM, **Fig. 2J**) is a long-chain, non-polar lipid found on the surface of *Mtb* and other pathogenic slow-growing mycobacteria (Daffé and Laneelle, 1988). It consists of a phthiocerol A backbone, connected to two methyl-branched fatty acids by ester linkages. Loss of PDIM is associated with

decreased virulence (Mulholland et al., 2023). Additionally, PDIM contributes to pathogenesis by promoting escape from phagolysosomes (Augenstreich et al., 2017; Barczak et al., 2017; Lerner et al., 2018; Quigley et al., 2017). Trehalose dimycolate (TDM, **Fig. 2F**), also known as cord factor, and trehalose monomycolate (TMM, **Fig. 2G**) are the most abundant glycolipids in *Mtb*. TDM consists of a trehalose head group connected to two MA tails through ester linkages, whereas TMM only contains one MA tail. TDM promotes *Mtb* survival by decreasing phagosomal acidification and phagolysosomal fusion in macrophages (Indrigo et al., 2003)**,** whereas strains lacking TDM exhibit reduced infectivity in vivo and survival in vitro (Bloch, 1950; Indrigo et al., 2002). Diacyl trehalose (DAT, **Fig. 2H**) consists of a trehalose headgroup with one steric acid tail and one mycosanoic acid tail. Pentacyl trehalose (PAT, **Fig. 2I**) consists of a trehalose headgroup with one steric acid tail and four mycolipenic acid tails. Sulfoglycolipid (SGL, **Fig. 2E**) consists of a sulfated trehalose headgroup with one palmitic acid tail, one phthioceranic acid tail, and two hydroxyphthioceranic acid tails. These lipid tails contain a varying number of methyl groups close to the headgroups. For decades, significant efforts have been made to elucidate the biosynthetic pathways of the trehalose-derived glycolipids (Kalscheuer and Koliwer-Brandl, 2014). Now that the composition of the mycomembrane is mostly known, an emerging question in the field is how this uniquely complex membrane dynamically protects the bacterium.

In lieu of expensive laboratory experiments restricted by biosafety considerations, researchers are increasingly adding computational simulations to their repertoires for studying biochemical systems. Molecular dynamics (MD) simulations employ Newton's equations of motion, along with descriptions of electrostatic and chemical interactions to simulate the motion of individual atoms with discrete time steps. Since the first simple MD simulations in the late 1950s, intense scientific efforts and advancements in computational power have increased the accuracy and size of these simulations many fold. In recent years, a variety of full bacterial cell envelopes have been successfully simulated, such as the AcrAB-TolC multidrug efflux pump embedded in the *Escherichia coli* cell envelope. Specifically, much effort has been devoted to modeling the cell envelope of Gram-negative bacteria (Khalid et al., 2022). Recent work has expanded to mycobacterial systems. For instance, transport mechanics of the Mycobacterial membrane protein large 3 (MmpL3) have been modelled via high-throughput virtual screening and MD simulations (Choksi et al., 2024). Additionally, the dynamic behavior of MAs in a variety of environments has been simulated, connecting their conformations and functional groups to differences in drug permeability (Basu et al., 2024; Groenewald et al., 2014; Vasyankin et al., 2024). The supramolecular organization of PIM lipids in the mycobacterial plasma membrane has been mapped, showing how these lipids cluster to modulate membrane fluidity and host-pathogen interactions (C. M. Brown et al., 2023; T. Brown et al., 2023). Finally, simulations of PDIM lipids demonstrated their conical shape promotes macrophage membrane remodeling, a key step in *Mtb* infection (Augenstreich et al., 2019).

Despite these advances, modeling the mycomembrane with MD simulations remains uniquely challenging due to its dense array of structurally diverse components, its complex spatial organization, and the paucity of resolved protein structures. To overcome these limitations and advance atomistic modeling of the mycobacterial envelope, we employed a three-step approach in this study. First, symmetric bilayers consisting of α-MAs in various starting conformations were simulated to elucidate whether they would form stable bilayers and to observe the various folding

patterns (**Fig. 2B-D**). Next, symmetric bilayers with various *Mtb*-specific glycolipids were simulated (**Fig. 2K**). Finally, the area-per-lipid (APL) values from the inner leaflet symmetric bilayers were used to construct asymmetric MOM bilayers with α-MAs in the inner leaflet, and six lipid types in the upper leaflet (**Fig. 2L**). The main goals of this study are to characterize the dynamics of mycobacterial lipids in realistic MOM bilayers and to elucidate the organizational structure of the mycomembrane. To the best of our knowledge, this study presents the first full atomistic models of the mycomembrane, an important step towards modeling the full mycobacterial cell envelope.

Results

α-Mycolic acid conformations dictate stability and thermal resilience in symmetric bilayers

The first set of simulations were run to characterize the stability of three conformations of α-MAs. We simulated three distinct bilayers, with MAs initially in fully extended (MA_eU), semi-folded (MA_sZ), or fully folded (MA_W) conformations (**Figs. 1-2**). These compositions were simulated at 313 K and 333 K to investigate the stability of α-MAs at high fever temperature. The simulation system name, compositions, and basic statistics are summarized in **Supporting Information Table S1**.

From our simulations, MA_eU (**Fig. 3A**) and MA_sZ (**Fig. 3D**) mostly maintained their initial conformations in the bilayers, while MA_W quickly unfolded into the sZ shape (**Fig. 3G**) by extending their long chains toward the midplane of the bilayer, encountering a barrier to interdigitation, and folding back into their own leaflet. This causes an increase in the membrane thickness (**Supporting Information Fig. S1A**). As shown in **Fig. 3E, 3H**, MA_sZ and MA_W have wider terminal carbon distributions than MA_eU, indicating a variety of conformations. When compared to the profiles from the MA_eU systems (**Fig. 3B**), there is significantly less interdigitation by the long chains of MA_sZ and MA_W. We believe that the barrier to interdigitation at the interleaflet space is due to L-shaped conformations, in which α-MA long chains first extend parallel to the bilayer normal, then undergo a sharp kink at the bilayer center, causing the carbons beyond the first cyclopropane ring to settle perpendicular to the bilayer normal. This leads to vertical heterogeneity in the bilayers with initially folded MAs. In **Fig. 3B, 3E,** and **3F**, drops in the order parameter profiles align well with the density of cyclopropane rings, indicating a bilayer disrupting effect. These trends are visually displayed in **Fig. 3C, 3F,** and **3I**, where snapshots of the three bilayer systems at 313 K are shown. In the MA_W snapshot (**Fig. 3I**), the terminal carbons of lipids from each leaflet are mixing at the interleaflet space, and do not interdigitate as much as in the MA_eU or MA_sZ systems. These results indicate that fully folded α-MAs cannot form a stable bilayer and prefer to be in extended conformations. This is substantiated by the time series of the membrane thickness (**Supporting Information Fig. S1A**), in which the MA_W bilayers do not reach a stable thickness even after 3 μs production. In the MA_eU systems, very few lipids transitioned to the sZ shape. In contrast, lipids in the MA_sZ system were able to transition to the eU shape. This asymmetry in conformational interconversion, in which sZ transitions to eU, but not vice versa, may reflect both thermodynamic preferences (e.g., lower energy barriers for sZ to eU) and the limited time scales of our simulations (3 μs production runs). While the MA_W system failed to equilibrate fully (**Supporting Information Fig.**

S1A), the lack of eU to sZ transitions in other systems could stem from kinetic trapping, where higher energy barriers or slower reorientation dynamics prevent sampling of these conversions within the simulation window.

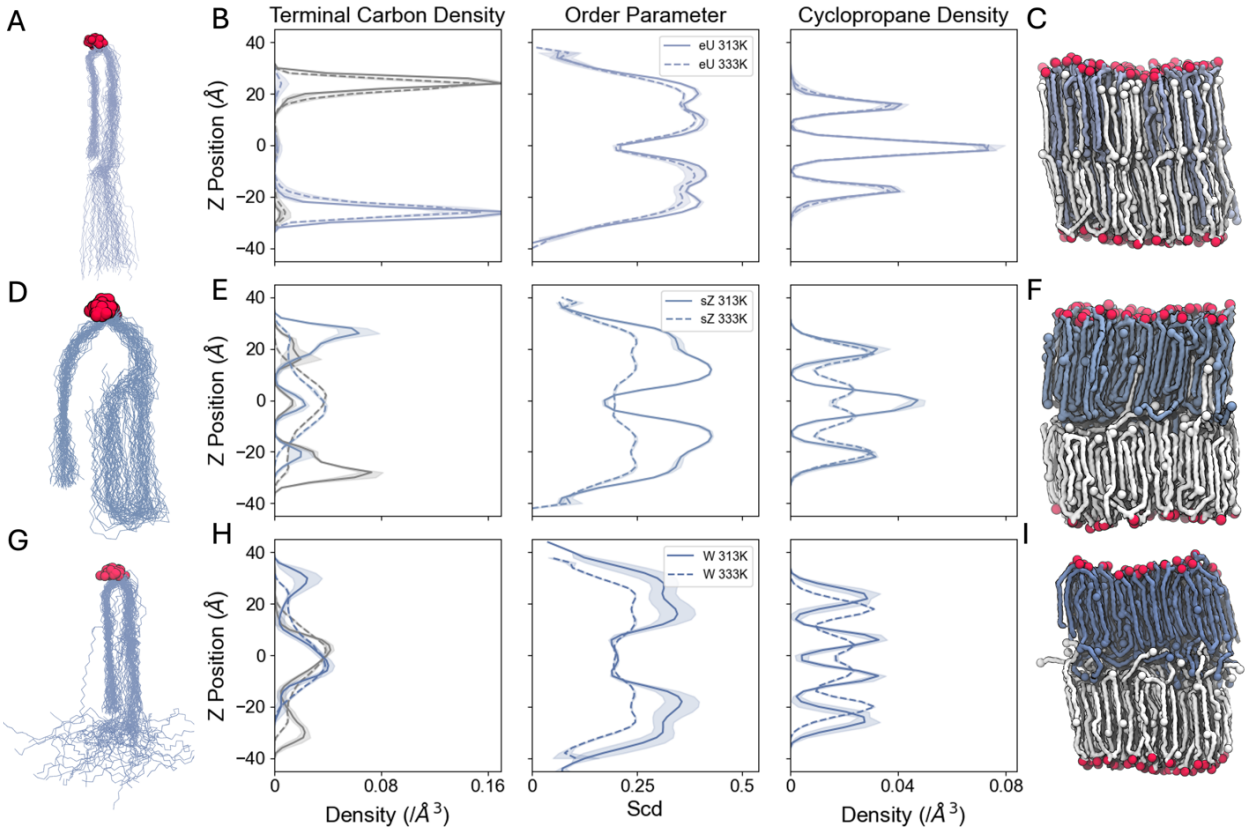

Figure 3. Folding patterns and organization of mycomembrane inner leaflet symmetric bilayers. A, D, G. Overlaid structures of one mycolic acid (**A**. MA_eU, **B**. MA_eZ, and **C**. MA_W) from every 10 frames of the final 500 ns production. Structures were aligned on 15 carbons at the top of the α-alkyl chain and 3 carbons at the top of the β-hydroxy chain: named C10 to C27 in the MA topologies. Oxygen atoms are displayed as red spheres. **B, E, H.** Lipid dynamics at 313 K (solid lines) and 333 K (dashed lines). The three columns are terminal carbon density profiles, average lipid order parameters of carbons (Vermeer et al., 2007), and cyclopropane density profiles in 2 Å-wide slabs along the z-axis (i.e., the membrane normal) with the bilayer center at z=0. For carbon density profiles, lipids belonging to the lower leaflet are depicted in grey and those from the upper leaflet are depicted in blue. **C, F, I.** Snapshots with varying initial compositions after 3 μs production. Lower leaflet lipids are shown in white, upper leaflet lipids are shown in light, medium, and dark blue. Oxygen atoms are displayed as red spheres. Terminal carbons and cyclopropane carbons are shown as spheres colored according to their leaflet.

To examine the temperature-dependence of α-MA folding, we simulated a symmetric bilayer of 60 MA_eU in each leaflet for 2 μs at 313, 323, 333, 338, 343, and 353 K. As temperature

increases, the average area per lipid (APL) increases linearly, while the membrane thickness decreases slightly (**Supporting Information Fig. S2**). From 323 K to 353 K, the average lateral diffusion coefficients of MAs increase linearly, showing faster dynamics at higher temperatures (**Fig. 4A**). The order parameter profiles of the long chain of MA show consistent drops in acyl chain order at the *proximal* and *distal* positions of the cyclopropane rings (**Fig. 4B, 3C**), consistent with the MA_sZ and MA_W bilayers. As the system temperature increases from 313 K to 333 K, the average order decreases slightly. At 338 K, the lipid order drops significantly, and there is a high standard deviation among replicas. The 343 K and 353 K bilayers show a significantly lower order between the cyclopropane rings than the lower temperature bilayers, suggesting a phase transition from liquid ordered to liquid disordered (**Fig. 4B**). Therefore, the transition temperature of bilayers with this composition appears to be close to 338 K in our simulations. Next, to understand how chain interdigitation changes as temperature increases, we produced z-density profiles of the terminal carbons (C75) from MAs and separated them by leaflet. As shown in **Fig. 4D**, bilayers from 313 K to 333 K show a consistent distribution, with all lipids reaching far into the opposite leaflet. At 338 K, the density plot has an intermediate distribution between the low and high temp simulated bilayers, indicating that 338 K may be close to the melting point of the bilayer. The 343 K and 353 K profiles (pink and cyan lines, respectively) indicate that a phase transition has occurred. The carbons below the second cyclopropane rings in each leaflet mix in the interleaflet space, inducing a melted phase. In these higher temperature systems, α-MAs are very dynamic, similar to lipids in a liquid disordered phase. Having established α-MAs' preference for extended conformations and contributions to bilayer stability, we next explored how outer leaflet lipids fine-tune membrane properties under shifting metabolic and environmental pressures.

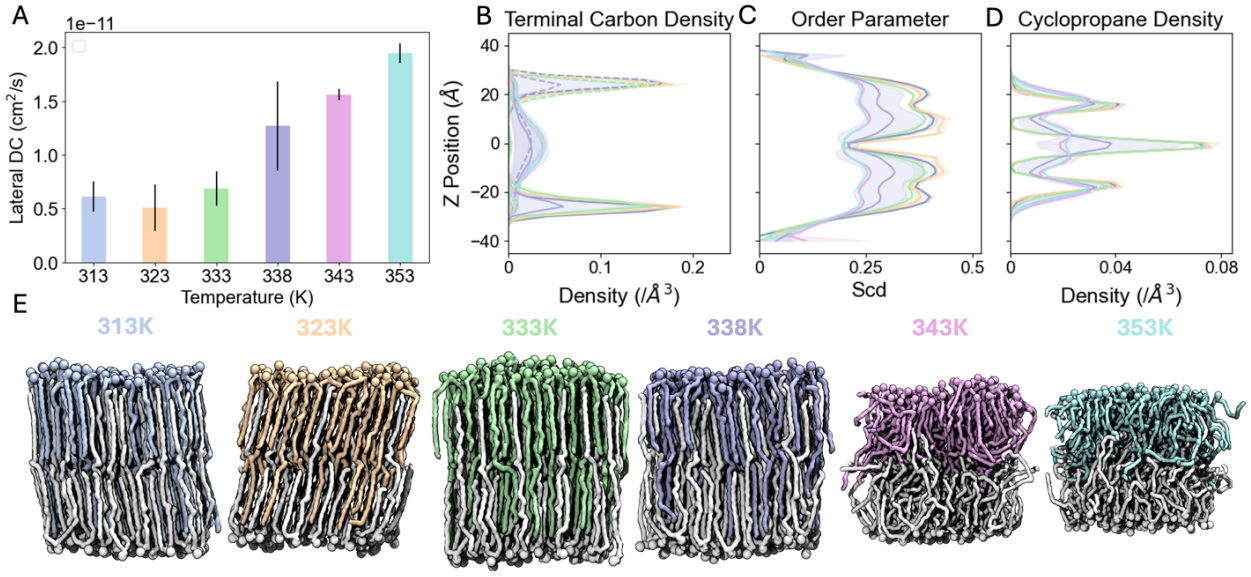

Figure 4. Phase transition of pure fully-extended α-mycolic acid bilayers. A. Lateral diffusion coefficients from 313 K to 353 K. **B**. Terminal carbon (C75) z-density profiles separated by leaflet along the temperature gradient. Upper leaflet lipids are shown with solid lines, and lower leaflet lipids shown with dashed lines. **C**. Average order parameters of MA at varying temperatures. **D**. Cyclopropane carbons (CC1, CC2) z-density profiles along the temperature gradient. **E**.

Snapshots along the temperature gradient, with lower leaflet lipids shown in white, upper leaflet lipids shown in colored lines, and oxygen atoms shown as spheres. Line and shaded area colors in **B**, **C**, and **D** correspond to those of upper leaflet lipids in **E**.

Outer leaflet lipids drive unexpected membrane heterogeneity and softness of the Mycomembrane

14 symmetric bilayer systems were simulated to investigate the effects of glycolipids in the mycomembrane outer leaflet (**Supporting Information Table S1**). The simulations have seven distinct compositions: one with all six glycolipids (**Fig. 2E-J**), and the other six with one glycolipid omitted, mimicking specific lipid knockout strains. Each lipid type contains a trehalose headgroup initially at the water-membrane interface and a variety of acyl or MA tails. PDIM, the only lipid type without a trehalose headgroup, is a nonpolar molecule, and has been shown to migrate into host epithelial membranes, promoting infectivity (Cambier et al., 2020). In a 2019 study, PDIM lipids were shown to adopt a conical shape, allowing them to aggregate in between the two leaflets of a POPC bilayer (Augenstreich et al., 2019). In our simulations, PDIM moves quickly into the membrane center, creating a distinct layer at the interleaflet space (**Fig. 5B, 5D**) and mimicking behavior from the previous study (Augenstreich et al., 2019). Surprisingly, some PAT lipid headgroups were also able to move into the bilayer center (**Fig. 5B, 5D**). PAT has a hydrophilic trehalose headgroup, so their migration into the membrane center was unexpected. Notably, PAT has five lipid chains, which is the most chains out of all the glycolipids included in the systems. Also, methylation near the top of the lipid tails may increase the equilibrium APL of PAT and promote movement away from the water-bilayer interface into the membrane. Although PAT also migrates to the bilayer midplane, the PAT-deficient bilayers did not exhibit reduced thickness as the PDIM-deficient thickness did (**Supporting Information Table S1**). This may be due to fewer PAT than PDIM moving to the bilayer midplane. In the All_Lipids systems, PDIM migrates first, bulging the upper leaflet and reducing lipid headgroup crowding (**Supporting Information Figs. S5, S6**). In this slightly less crowded environment, hydrophobic forces from PAT's tails overcome the hydrophilic forces from the trehalose headgroup, causing some PATs to move deeper into the hydrophobic region. We also observed a stark difference in the speed with which PDIM and PAT migrate to the center at different temperatures. PDIM molecules do not fully aggregate at the membrane center until about 1500 ns at 313K, whereas they accumulate within 500ns at 333K (**Fig. 5B, 5D**). This can be attributed to higher kinetics at 333K, causing the lipids to move faster. Coarse-grained models may be sufficient to observe full aggregation of hydrophobic species at the membrane midplane at lower temperatures. In the bilayers with no PDIM, less PAT migrates to the center, suggesting a link between induced disorder by PDIM and PAT migration (**Supporting Information Figs. S5, S6**). In all symmetric outer leaflet simulations, PDIM and PAT sit just below the headgroups of other lipids at the start of production, due to our equilibration scheme. During the last step of equilibration, lipid headgroups are allowed to move freely, which initiates migration to the membrane center and causes the slight difference between PDIM/PAT and the other lipids' headgroup positions (**Supporting Information Figs. S5, S6**). To observe how this migration affects the fluidity of these lipids, we plotted the average order parameters of carbon atoms along the z-axis, and found low lipid order, with a slight valley at +/- 10 Å from the bilayer center (**Fig. 5F**). In fact, there was little to no difference in lipid order between

313 K and 333 K in any lipid type (**Supporting Information Fig. S4E**). Additionally, in SGL-deficient bilayers, fewer PDIMs and PATs move to the bilayer midplane. This may be due to the highly methylated lipid tails of SGL. When present in the bilayer, these methyl groups may disrupt lipid packing and increase fluidity, allowing more PDIMs to move into the hydrophobic region. **Supporting Information Figure S8** shows the average lipid order parameter along each lipid tail for all outer leaflet symmetric systems. Without SGL, lipid tails are consistently more ordered, supporting the notion that SGL's methylated tails are disrupting lipid packing. Further studies are necessary to investigate the effect of glycolipid-deficient compositions on the dynamic properties of the asymmetric MOM.

The migration of PDIM and PAT into the interleaflet space disrupts lipid packing in the outer leaflet, creating localized regions of structural disorder. While these perturbations modestly elevate lateral diffusion coefficients compared to tightly packed regions, a signature of reduced packing efficiency, the absolute diffusion values remain strikingly low relative to typical lipid bilayers (**Fig. 5E**) (Almeida et al., 2005). This suggests that while lipid mobility increases at disordered sites, lateral movement across the membrane remains constrained, likely due to persistent interactions between long-chain mycolic acids or residual ordered domains. To bridge insights from symmetric bilayer simulations with the native mycomembrane, we constructed asymmetric bilayers replicating its architectural complexity.

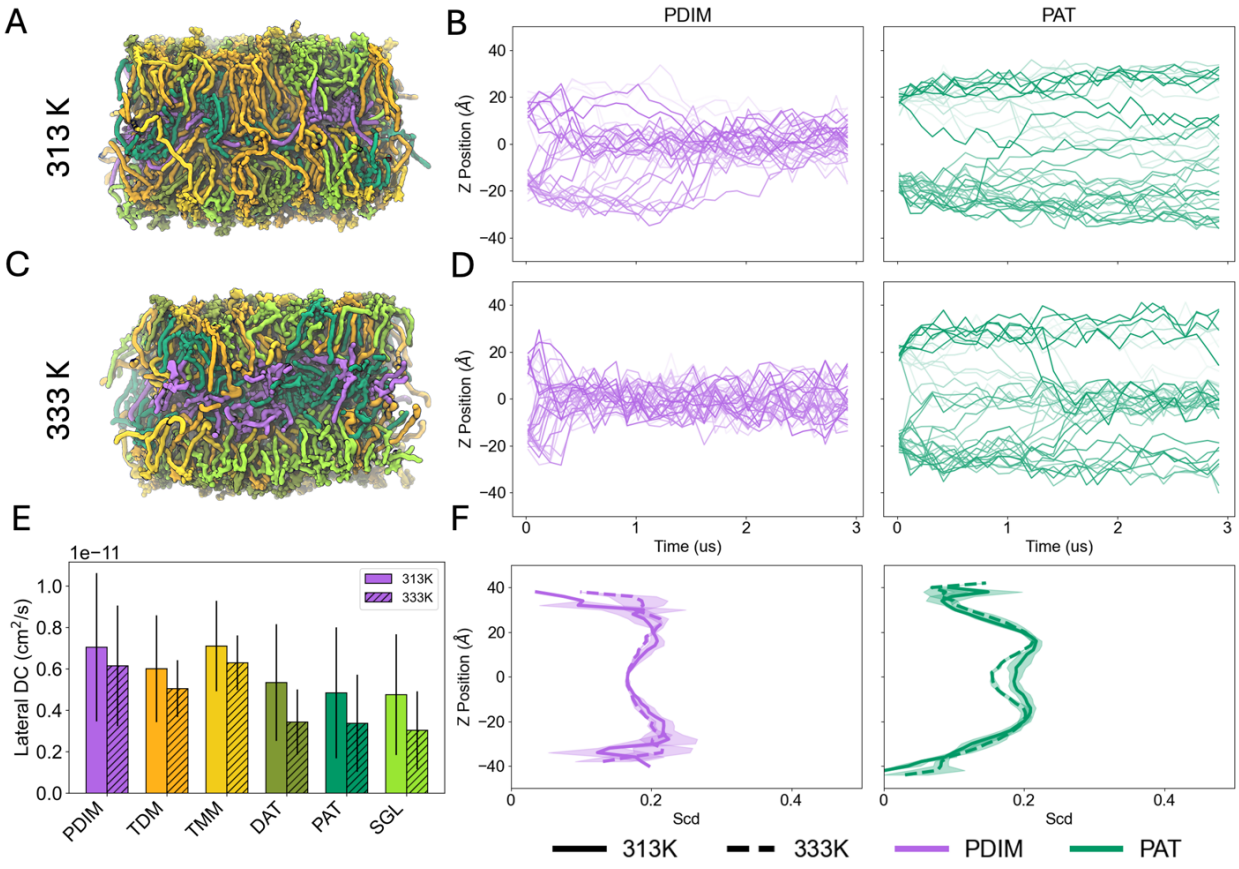

Figure 5. Lipid aggregation in mycomembrane outer leaflet symmetric bilayers. A, C. Snapshots of All_Lipids systems after 3 μs production at 313 K and 333 K, respectively (see **Supporting Information Table S1** for system name, composition, and basic statistics). Lipid colors match the coloring from **Fig. 2**. Water and ions are omitted for clarity. **B, D**. Headgroup z position time series of PDIM (purple) and PAT (green) at 313 K and 333 K, respectively. Each line is a separate lipid molecule. **E**. Lateral diffusion coefficients from All_Lipids system for each lipid type. Solid bars are from the 313 K system, and hatched bars are from the 333 K system. Error bars are the standard errors across 3 replicas. **F**. Comparison of average deuterium order parameters of carbons along the z-axis for PDIM (light purple) and PAT (light green) at 313 K (solid lines) and 333 K (dashed lines). Shaded regions are the standard errors across 3 replicas. All analysis is averaged over the last 500 ns production.

Asymmetric mycomembrane presents a phase transition from disordered outer leaflet to ordered inner leaflet

Simulating asymmetric bilayers presents a fundamental challenge: the intrinsic APL mismatch between leaflets with distinct lipid compositions. In asymmetric systems, differential packing of lipids in each leaflet can lead to bilayer instability, curvature, or defects if initial APLs are not carefully chosen (Bodosa et al., 2024; Park et al., 2021). For the mycomembrane, this challenge is compounded by the dynamic behavior of outer-leaflet glycolipids, such as PDIM and PAT, which migrate into the interleaflet space and disrupt conventional APL calculations (**Supporting Information Figs. S5, S6**). Specifically, Voronoi tessellation, a common method for estimating APLs, fails in these systems due to irregular spatial distribution and overlapping lipid tails. To address this, we calculated APLs from stable symmetric bilayers of α-MAs and adjusted the total lipid count in the asymmetric system to match the equilibrium APL of the outer-leaflet glycolipid ensemble (All_Lipids_313, see **Supporting Information Table S1**). The final asymmetric bilayer comprised 94 MA_eU, 47 MA_sZ, and 47 MA_W lipids in the lower leaflet, with 20 molecules of each glycolipid type in the upper leaflet. Although this model does not perfectly reflect a physiological composition of the mycomembrane as native mycomembranes have more TDM than TMM and PDIM, as well as a variety of MA classes in the inner leaflet, we believe that this composition is a good starting point, leading a way to more accurate models. This configuration was simulated for 3 μs at both 313 K and 333 K (**Fig. 6A, 6C**), followed by analysis of temperature-dependent lipid dynamics.

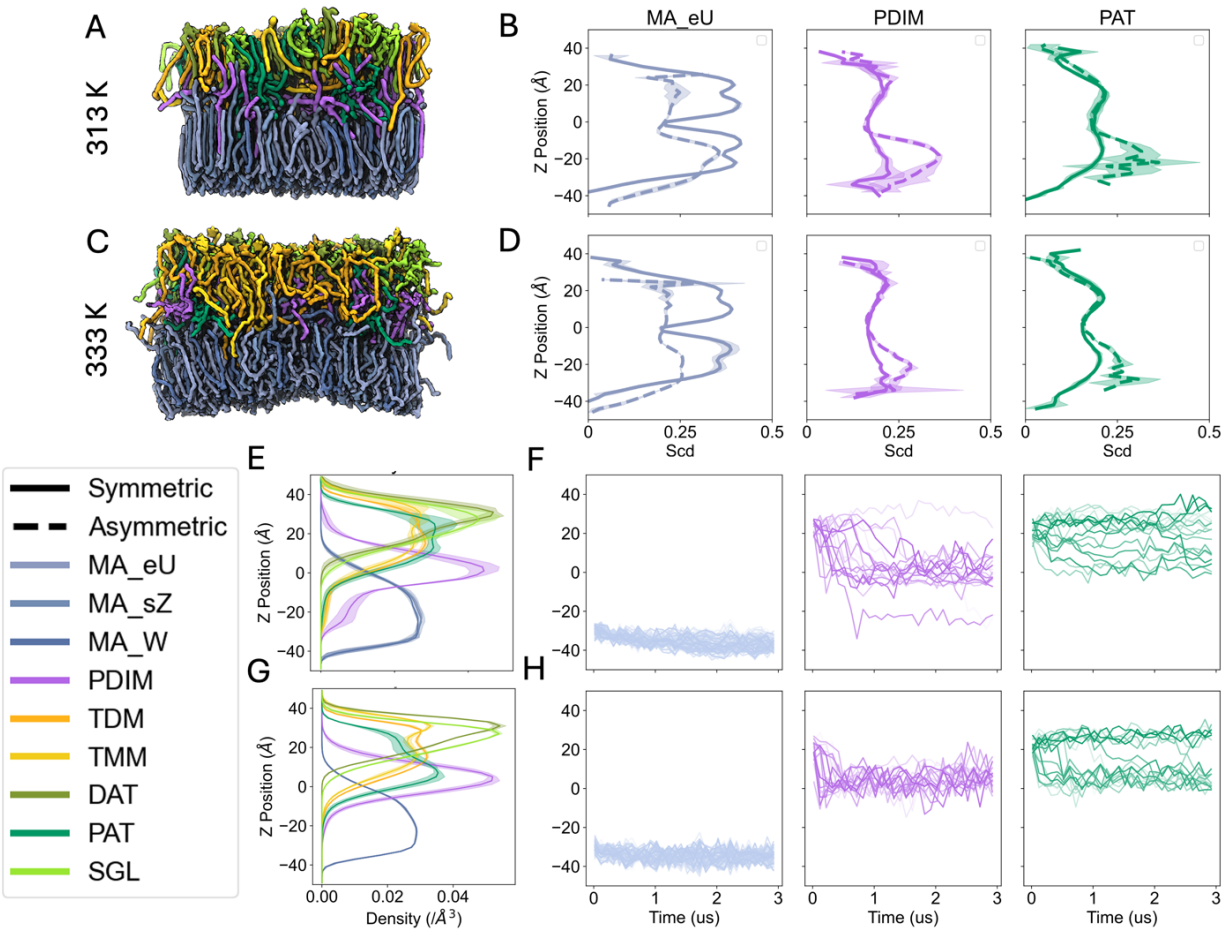

Figure 6. Vertical heterogeneity and lipid dynamics in asymmetric mycomembranes. A, C. Snapshots after 3 μs production at 313 K and 333 K, respectively. Lipid colors match the coloring from **Fig. 2**, and lipids are shown with the QuickSurf drawing method. **B, D**. Comparison of average deuterium order parameters of carbons along the z-axis for MA_eU (light blue), PDIM (light purple), and PAT (light green) at 313 K and 333 K, respectively. Solid lines are from the symmetric systems and dashed lines are from the asymmetric systems. **E, G**. Full lipid z-density profiles for each lipid at 313 K and 333 K, respectively. Shaded regions are the standard errors across 3 replicas. **F, H**. Headgroup z position time series of MA_eU (light blue), PDIM (light purple), and PAT (light green) at 313 K and 333 K, respectively. Each line is a separate lipid molecule. All analysis is averaged over the last 500 ns of production.

We first calculated the average order parameter along the z-axis. When comparing the symmetric systems to the asymmetric system, we see a slight decrease in the order parameters for inner leaflet lipids at 313 K and a sharp decrease at 333 K (**Fig. 6B, 6D**). Interestingly, PDIM and PAT, which also migrate to the bilayer center in the asymmetric systems, exhibit higher order in the inner leaflet. In fact, TDM and TMM also adopt a higher order when they reach into the inner leaflet (**Supporting Information Fig. S7C-D**). Full lipid z-density profiles (**Fig. 6E, 6G**), along with headgroup z-position time series, show that most of the PDIM molecules are settling

in the interleaflet space (**Fig. 6F, 6H**). Closer analysis reveals that PDIM lipids can fully flip-flop into the MA-rich inner leaflet, with some headgroups lining up with the upper bounds of the MA_eU headgroups. This suggests that, at thermodynamic equilibrium, the outer membrane of *Mtb* maintains heterogeneous fluidity, and PDIM migration to the membrane center is disrupting the deep interdigitation that stabilizes pure α-MA bilayers, allowing for a disordered outer leaflet. This unique membrane architecture has important implications for the resilience of *Mtb* in various growth states and host environments, which is elaborated below.

Discussion

Our simulations of pure α-MA bilayers have revealed important dynamic behaviors that give evidence for resistance to passive diffusion and high thermal resilience. In contrast to common phospholipids, which have much shorter tails, α-MAs have a higher transition temperature. Such longer lipid tails have more surface area, increasing the strength of van der Waals interactions and raising their transition temperatures (Rawicz et al., 2000). This trend is consistent with our results. Additionally, the high degree of interdigitation prevents free lateral diffusion, further raising the melting temperature. Above 338 K, the degree of interdigitation drops and fluidity increases. The extended conformation of α-MAs and their phase transition near 338 K (~65°C) in our simulations reflect a nuanced adaptation in *Mtb*. While this transition temperature exceeds host fever ranges (310–315 K), its biological significance may lie less in fever resistance and more in mitigating environmental stresses. Notably, the rigidity of MA-rich bilayers likely has evolved to withstand desiccation, critical for survival in aerosols during transmission, rather than extreme heat. This ordered structure creates a formidable barrier against antibiotics and host defenses, but its functionality extends further; under stasis conditions (e.g., hypoxia, caseum), *Mtb* downregulates trehalose dimycolate (TDM) production, potentially mimicking a membrane with fewer surface-exposed glycolipids (Hunter et al., 2006). Such metabolic adaptations could reduce fluidity, favoring a liquid ordered phase that further restricts permeability and sustains dormancy. A static, overly rigid membrane might fracture under stress, while excessive fluidity would permit drug entry. Based on our simulations, cyclopropane groups in MAs may balance these extremes, enabling structural flexibility without compromising impermeability. This "dynamic resilience" explains *Mtb*'s resistance to small molecules; drugs targeting fluid membranes fail against the mycomembrane's adaptive plasticity (Modak et al., 2022). Importantly, the mycomembrane's adaptability underscores its vulnerability. Therapies disrupting MA cyclopropanation or folding dynamics could destabilize this equilibrium, collapsing the barrier.

The outer leaflet symmetric bilayers, comprised of trehalose-derived glycolipids and PDIMs, reveal PDIM-dependent thickness. As observed in both symmetric outer leaflet systems and asymmetric systems, PDIM migrates to the bilayer midplane, causing the upper leaflet to bulge and increasing the overall thickness. Reduced thickness in the systems lacking PDIM, an important virulence factor for *Mtb*, may allow for higher nutrient uptake. This corroborates a 2009 study in which Domenech and Reed found a correlation between PDIM absence *in vitro* and attenuated virulence (Domenech and Reed, 2009). Although PAT also migrates to the bilayer midplane, the PAT-deficient bilayers did not exhibit reduced thickness as the PDIM-deficient thickness did. This may be due to fewer PAT than PDIM moving to the bilayer midplane. In the All_Lipids systems, PDIM migrates first, bulging the upper leaflet and reducing lipid headgroup

crowding. In this slightly less crowded environment, hydrophobic forces from PAT's tails overcome the hydrophilic forces from the trehalose headgroup, causing some PATs to move deeper into the hydrophobic region. Additionally, in SGL-deficient bilayers, fewer PDIMs and PATs move to the bilayer midplane. This may be due to the highly methylated lipid tails of SGL. When present in the bilayer, these methyl groups may disrupt lipid packing and increase fluidity, allowing more PDIMs to move into the hydrophobic region. **Supporting Information Figure S8** shows the average lipid order parameter along each lipid tail for all outer leaflet symmetric systems. Without SGL, lipid tails are consistently more ordered, supporting the notion that SGL's methylated tails are disrupting lipid packing. Further studies are necessary to investigate the effect of glycolipid-deficient compositions on the dynamic properties of the asymmetric MOM.

The asymmetric architecture of the mycobacterial outer membrane (MOM) establishes a vertical heterogeneity that underpins its unique biophysical and functional properties. The inner leaflet, composed of MAs, maintains a liquid ordered phase, while the outer leaflet, composed of loosely packed PDIMs and trehalose-derived glycolipids, retains a liquid disordered phase. This fluidity gradient diverges from conventional membrane systems, where disordered leaflets typically undergo induced ordering via interactions with adjacent ordered layers (Feigenson et al., 2023). In *Mtb*, however, PDIM and PAT disrupt interleaflet coupling, stabilizing vertical heterogeneity. Critically, this localized disorder in the outer leaflet may enable lipid shedding events, such as the release of immunomodulatory TDM. The heightened mobility of lipids in disordered domains could destabilize their membrane anchorage, allowing dissociation driven by mechanical instability and thermal fluctuations. While direct observation of shedding remains beyond current simulation resolution, this mechanism could reconcile *Mtb's* impermeability with its ability to dynamically interact with host immune systems, i.e., shedding lipids to modulate immunity while retaining barrier integrity. This vertical fluidity gradient contrasts with eukaryotic plasma membranes, which sustain functional asymmetry through cholesterol enrichment in the outer leaflet to stabilize microdomains (Doktorova et al., 2025; Ikeda et al., 2006). Unlike cholesterol-dependent eukaryotes, *Mtb* achieves its asymmetry through MA rigidity and outer leaflet lipid-driven disorder, bypassing sterols. The resulting "rigid yet adaptive" architecture balances global impermeability with localized plasticity, permitting spatially restricted lipid rearrangements, which may aid in pathogenicity by TDM shedding at host interaction. Such compartmentalization would allow *Mtb* to fine-tune immune evasion while resisting small-molecule penetration.

The MOM's design further diverges from Gram-negative bacterial outer membranes, which rely on lipopolysaccharide (LPS)-stiffened outer leaflets and porin-mediated transport (Nikaido, 2003; Silhavy et al., 2010). While Gram-negative bacteria employ porins for selective permeability and efflux pumps for antibiotic resistance, *Mtb* lacks porins and instead relies on its densely packed, interdigitated MA layer to limit passive diffusion. Recent studies propose that PE/PPE proteins may act as selective transporters, suggesting a need for updated models integrating protein-lipid cooperativity (Babu Sait et al., 2022; Boradia et al., 2022). Moreover, the MOM's unique thermal resilience, evidenced by its ~338 K phase transition, may stem from cyclopropane modifications in α-MA chains that modulate fluidity without sacrificing structural coherence. This contrasts with Gram-negative bacteria's outer membranes, where LPS rigidity in the outer leaflet and phospholipid fluidity in the inner leaflet are spatially segregated between leaflets (Im and

Khalid, 2020; Wu et al., 2014). *Mtb's* vertical heterogeneity thus represents an evolutionary innovation, enabling simultaneous thermal adaptation and pathogenicity.

Future studies should prioritize elucidating lipid trafficking mechanisms across the MOM's asymmetric leaflets, particularly how PDIMs and other lipids transit from outer to inner leaflets or vice versa, despite MA interdigitation. Computational models incorporating PE/PPE proteins could reveal dynamic protein-lipid interactions governing selective transport or shedding. Additionally, coarse-grained models of the outer membrane could aid in drug-transport studies, potentially revealing energetic pathways by which novel antibiotics penetrate the complex cell envelope over larger timescales. Therapeutically, disrupting lipid clustering at the interleaflet interface or inhibiting enzymes responsible for MA cyclopropanation could destabilize the fluidity gradient, rendering *Mtb* vulnerable to antibiotic penetration while impairing immune evasion. Additionally, outer membranes of other mycobacteria can be modeled using the framework described here. For instance, adding unsaturated lipids and trehalose polyphleates while omitting PAT would allow researchers to investigate the unique properties of *Mycobacterium abscessus.* By bridging molecular-scale asymmetry with organism-scale resilience, this model advances our understanding of how *Mtb's* mycomembrane achieves extraordinary adaptability.

Methods

System and Simulation Parameters

All bilayer systems were constructed using *CHARMM-GUI Membrane Builder* (Feng et al., 2023; Jo et al., 2009), and were simulated using *OpenMM* version 8.2 under periodic boundary conditions (Eastman et al., 2024). The inner leaflet symmetric bilayers comprised α-MAs with 78 carbons, initialized in extended (eU), semi-folded (sZ), or fully folded (W) conformations (**Fig. 2B-D, Supporting Information Table S1**). Outer leaflet symmetric bilayers included six *Mtb*-specific glycolipids: PDIM, TDM, TMM, DAT, PAT, and SGL (**Fig. 2E-J**, **Supporting Information Table S1**), with compositions validated against experimental ratios (Chiaradia et al., 2017). Asymmetric bilayers combined MA-rich inner leaflets (94 eU, 47 sZ, 47 W MAs) and glycolipid-rich outer leaflets (20 lipids per type). Each system was solvated in a 150 mM KCl solution using the TIP3P water model (Jorgensen et al., 1983) and neutralized with counterions. Force field parameters for MAs and glycolipids were derived from the *CHARMM36* lipid force field (Klauda et al., 2010), with cyclopropane ring parameters validated against prior simulations (Poger and Mark, 2015). Following *Membrane Builder*'s default six-step equilibration protocol (Jo et al., 2009, 2007), the NVT (constant particle number, volume, and temperature) dynamics was first applied with a 1 femtosecond (fs) time step for 250 picoseconds (ps). Subsequently, the NPT (constant particle number, pressure, and temperature) ensemble was applied with a 1 fs time step (for 125 ps) and with a 2 fs time step (for 1.5 ns). During the equilibration, positional and dihedral restraint potentials were applied to lipid and water molecules, and their force constants were gradually reduced. With no restraints, we performed 3 μs production for 3 replicas of each system using 4 fs timestep. Hydrogen mass repartitioning method was used together with the SHAKE algorithm to constrain the bonds containing hydrogen atoms (Ryckaert et al., 1977). The van der Waals interactions were cutoff at 12 Å with a force-switching function between 10 and 12 Å (Steinbach and Brooks, 1994), and electrostatic interactions were calculated by the particle-mesh Ewald

method (Essmann et al., 1995). The temperature and pressure (at 1 bar) were controlled by Langevin dynamics with a friction coefficient of 1 ps^{-1} and a semi-isotropic Monte Carlo barostat, respectively (Åqvist et al., 2004; Chow and Ferguson, 1995).

Bilayer Visualizations

Structural snapshots were rendered using *VMD 1.9.4* (Humphrey et al., 1996). Lipids were visualized with the *QuickSurf* drawing method to emphasize packing density, and oxygen atoms were highlighted as van der Waals spheres. For alignment of α-MA conformations (**Fig. 3A, 3D, 3G**), C10–C27 carbons of the β-hydroxy chain were used as reference points. Lipid colors matched initial configurations (**Fig. 2**) to ensure consistency across the figures.

Bilayer Analysis

System Width The system width of the simulation box was defined as the range of x values of the system at each time step. The average values in **Supporting Information Table S1** are an average over the final 500 ns of each replica.

Membrane Thickness The hydrophobic membrane thickness was measured as the distance between the average z-positions of the first carbon in each lipid tail (C24 and C27 in MA-containing lipids; C1 in other lipids) from opposing leaflets.

APL (Area Per Lipid) The APL was calculated by dividing the system's XY area at each time step by the number of lipids in each leaflet. The values in **Supporting Information Table S1** are an average over the final 500 ns of each replica.

Z-Density Profiles The mass density profiles along the bilayer normal (z-axis) were generated using an in-house python script, with a 1 Å resolution. Terminal carbons (C75 of MAs), cyclopropane rings, and glycolipid headgroups were resolved separately.

Scd vs Z Profiles Deuterium order parameters (S_{CD}) were computed using an in-house python script with values averaged over the final 500 ns. S_{CD} was calculated for all acyl carbons in the tails of each lipid type and binned into 2 Å slabs along the z-axis, using the following equation.

$$S_{CD} = \frac{\langle 3\,cos^2\,\theta - 1\rangle}{2}$$

where, θ is the angle between the C-H bond vector and the bilayer normal. The angular brackets represent temporal and molecular ensemble averages.

Lateral Diffusion Coefficients The lateral diffusion coefficients (D) were calculated from the mean squared displacement (MSD) using the Einstein relation:

$$D = \frac{1}{4}\lim_{t\to\infty}\frac{d}{dt}\langle|r(t) - r(0)|^2\rangle$$

MSD calculations were performed using MDAnalysis for the final 100 ns of simulation with a 10 ns lag time. The z-component of position was excluded to isolate lateral motions.

Acknowledgements:

This work is supported by the CNRS-MITI grant "Modélisation du vivant" 2020 (to M.C.), NSF MCB-2111728, and NIH R35 GM153458 (to W.I.). We thank Dr. Seonghoon Kim and Emanuel Luna for creating the topology and parameter files of the lipids in this study. We also thank Dr. Vivek Thacker and Dr. Gregor Weiss for invaluable discussions on the biological relevance of our simulations.

Author Contributions

T.P.B., M.C., and W.I. designed the research. T.P.B. performed the research and drafted the paper with input from the co-authors. M.C. and W.I.. helped with interpretation of results and substantially revised the manuscript.

References:

Almeida PFF, Vaz WLC, Thompson TE. 2005. Lipid Diffusion, Free Area, and Molecular Dynamics Simulations. *Biophys J* **88**:4434–4438. doi:10.1529/biophysj.105.059766

Åqvist J, Wennerström P, Nervall M, Bjelic S, Brandsdal BO. 2004. Molecular dynamics simulations of water and biomolecules with a Monte Carlo constant pressure algorithm. *Chemical Physics Letters* **384**:288–294. doi:10.1016/j.cplett.2003.12.039

Augenstreich J, Arbues A, Simeone R, Haanappel E, Wegener A, Sayes F, Le Chevalier F, Chalut C, Malaga W, Guilhot C, Brosch R, Astarie-Dequeker C. 2017. ESX-1 and phthiocerol dimycocerosates of Mycobacterium tuberculosis act in concert to cause phagosomal rupture and host cell apoptosis. *Cellular Microbiology* **19**:e12726. doi:10.1111/cmi.12726

Augenstreich J, Haanappel E, Ferré G, Czaplicki G, Jolibois F, Destainville N, Guilhot C, Milon A, Astarie-Dequeker C, Chavent M. 2019. The conical shape of DIM lipids promotes Mycobacterium tuberculosis infection of macrophages. *Proceedings of the National Academy of Sciences* **116**:25649–25658. doi:10.1073/pnas.1910368116

Babu Sait MR, Koliwer-Brandl H, Stewart JA, Swarts BM, Jacobsen M, Ioerger TR, Kalscheuer R. 2022. PPE51 mediates uptake of trehalose across the mycomembrane of Mycobacterium tuberculosis. *Sci Rep* **12**:2097. doi:10.1038/s41598-022-06109-7

Barczak AK, Avraham R, Singh S, Luo SS, Zhang WR, Bray M-A, Hinman AE, Thompson M, Nietupski RM, Golas A, Montgomery P, Fitzgerald M, Smith RS, White DW, Tischler AD, Carpenter AE, Hung DT. 2017. Systematic, multiparametric analysis of Mycobacterium tuberculosis intracellular infection offers insight into coordinated virulence. *PLOS Pathogens* **13**:e1006363. doi:10.1371/journal.ppat.1006363

Basu S, Mandal S, Maiti PK. 2024. Permeability of TB drugs through the mycolic acid monolayer: a tale of two force fields. *Phys Chem Chem Phys* **26**:21429–21440. doi:10.1039/D4CP02659D

Bloch H. 1950. STUDIES ON THE VIRULENCE OF TUBERCLE BACILLI : ISOLATION AND BIOLOGICAL PROPERTIES OF A CONSTITUENT OF VIRULENT ORGANISMS. *Journal of Experimental Medicine* **91**:197–218. doi:10.1084/jem.91.2.197

Bodosa J, Pane AJ, Klauda JB. 2024. Chapter Five - Modeling asymmetric cell membranes at all-atom resolution In: Deserno M, Baumgart T, editors. Methods in Enzymology, Biophysical Approaches for the Study of Membrane Structure—Part B: Theory and Simulations. Academic Press. pp. 157–174. doi:10.1016/bs.mie.2024.03.009

Boradia V, Frando A, Grundner C. 2022. The Mycobacterium tuberculosis PE15/PPE20 complex transports calcium across the outer membrane. *PLoS Biol* **20**:e3001906. doi:10.1371/journal.pbio.3001906

Brown CM, Corey RA, Grélard A, Gao Y, Choi YK, Luna E, Gilleron M, Destainville N, Nigou J, Loquet A, Fullam E, Im W, Stansfeld PJ, Chavent M. 2023. Supramolecular organization and dynamics of mannosylated phosphatidylinositol lipids in the mycobacterial plasma membrane. *Proceedings of the National Academy of Sciences* **120**:e2212755120. doi:10.1073/pnas.2212755120

Brown T, Chavent M, Im W. 2023. Molecular Modeling and Simulation of the Mycobacterial Cell Envelope: From Individual Components to Cell Envelope Assemblies. *J Phys Chem B* **127**:10941–10949. doi:10.1021/acs.jpcb.3c06136

Cambier C, Banik SM, Buonomo JA, Bertozzi CR. 2020. Spreading of a mycobacterial cell-surface lipid into host epithelial membranes promotes infectivity. *eLife* **9**:e60648. doi:10.7554/eLife.60648

Chiaradia L, Lefebvre C, Parra J, Marcoux J, Burlet-Schiltz O, Etienne G, Tropis M, Daffé M. 2017. Dissecting the mycobacterial cell envelope and defining the composition of the native mycomembrane. *Sci Rep* **7**:12807. doi:10.1038/s41598-017-12718-4

Choksi H, Carbone J, Paradis NJ, Bennett L, Bui-Linh C, Wu C. 2024. Novel Inhibitors to MmpL3 Transporter of Mycobacterium tuberculosis by Structure-Based High-Throughput Virtual Screening and Molecular Dynamics Simulations. *ACS Omega* **9**:13782–13796. doi:10.1021/acsomega.3c08401

Chow K-H, Ferguson DM. 1995. Isothermal-isobaric molecular dynamics simulations with Monte Carlo volume sampling. *Computer Physics Communications* **91**:283–289. doi:10.1016/0010-4655(95)00059-O

Daffé M, Laneelle MA. 1988. Distribution of Phthiocerol Diester, Phenolic Mycosides and Related Compounds in Mycobacteria. *Microbiology* **134**:2049–2055. doi:10.1099/00221287-134-7-2049

Dartois V, Dick T. 2024. Therapeutic developments for tuberculosis and nontuberculous mycobacterial lung disease. *Nat Rev Drug Discov* **23**:381–403. doi:10.1038/s41573-024-00897-5

Doktorova M, Symons JL, Zhang X, Wang H-Y, Schlegel J, Lorent JH, Heberle FA, Sezgin E, Lyman E, Levental KR, Levental I. 2025. Cell membranes sustain phospholipid imbalance via cholesterol asymmetry. *Cell*. doi:10.1016/j.cell.2025.02.034

Domenech P, Reed MB. 2009. Rapid and spontaneous loss of phthiocerol dimycocerosate (PDIM) from Mycobacterium tuberculosis grown in vitro: implications for virulence studies. *Microbiology (Reading)* **155**:3532–3543. doi:10.1099/mic.0.029199-0

Eastman P, Galvelis R, Peláez RP, Abreu CRA, Farr SE, Gallicchio E, Gorenko A, Henry MM, Hu F, Huang J, Krämer A, Michel J, Mitchell JA, Pande VS, Rodrigues JP, Rodriguez-Guerra J, Simmonett AC, Singh S, Swails J, Turner P, Wang Y, Zhang I, Chodera JD, De Fabritiis G, Markland TE. 2024. OpenMM 8: Molecular Dynamics Simulation with Machine Learning Potentials. *J Phys Chem B* **128**:109–116. doi:10.1021/acs.jpcb.3c06662

Essmann U, Perera L, Berkowitz ML, Darden T, Lee H, Pedersen LG. 1995. A smooth particle mesh Ewald method. *The Journal of Chemical Physics* **103**:8577–8593. doi:10.1063/1.470117

Feigenson GW, Huang J, Enoki TA. 2023. An Unexpected Driving Force for Lipid Order Appears in Asymmetric Lipid Bilayers. *J Am Chem Soc* **145**:21717–21722. doi:10.1021/jacs.3c05081

Feng S, Park S, Choi YK, Im W. 2023. CHARMM-GUI Membrane Builder: Past, Current, and Future Developments and Applications. *J Chem Theory Comput* **19**:2161–2185. doi:10.1021/acs.jctc.2c01246

Global Tuberculosis Report 2024. n.d. https://www.who.int/teams/global-tuberculosis-programme/tb-reports/global-tuberculosis-report-2024

Groenewald W, Baird MS, Verschoor JA, Minnikin DE, Croft AK. 2014. Differential spontaneous folding of mycolic acids from *Mycobacterium tuberculosis*. *Chemistry and Physics of Lipids* **180**:15–22. doi:10.1016/j.chemphyslip.2013.12.004

Groenewald W, Parra-Cruz RA, Jäger CM, Croft AK. 2019. Revealing solvent-dependent folding behavior of mycolic acids from Mycobacterium tuberculosis by advanced simulation analysis. *J Mol Model* **25**:68. doi:10.1007/s00894-019-3943-5

Hasegawa T. 2004. Structural analysis of biological aliphatic compounds using surface-enhanced Fourier transform Raman spectroscopy. *Biopolymers* **73**:457–462. doi:10.1002/bip.10556

Hasegawa T, Leblanc RM. 2003. Aggregation properties of mycolic acid molecules in monolayer films: a comparative study of compounds from various acid-fast bacterial species. *Biochimica et Biophysica Acta (BBA) - Biomembranes* **1617**:89–95. doi:10.1016/j.bbamem.2003.09.008

Humphrey W, Dalke A, Schulten K. 1996. VMD: Visual molecular dynamics. *Journal of Molecular Graphics* **14**:33–38. doi:10.1016/0263-7855(96)00018-5

Hunter RL, Olsen MR, Jagannath C, Actor JK. 2006. Multiple Roles of Cord Factor in the Pathogenesis of Primary, Secondary, and Cavitary Tuberculosis, Including a Revised Description of the Pathology of Secondary Disease. *Ann Clin Lab Sci* **36**:371–386.

Ikeda M, Kihara A, Igarashi Y. 2006. Lipid asymmetry of the eukaryotic plasma membrane: functions and related enzymes. *Biol Pharm Bull* **29**:1542–1546. doi:10.1248/bpb.29.1542

Im W, Khalid S. 2020. Molecular Simulations of Gram-Negative Bacterial Membranes Come of Age. *Annual Review of Physical Chemistry* **71**:171–188. doi:10.1146/annurev-physchem-103019-033434

Indrigo J, Hunter RL, Actor JK. 2003. Cord factor trehalose 6,6'-dimycolate (TDM) mediates trafficking events during mycobacterial infection of murine macrophages. *Microbiology* **149**:2049–2059. doi:10.1099/mic.0.26226-0

Indrigo J, Hunter RL, Actor JK. 2002. Influence of trehalose 6,6’-dimycolate (TDM) during mycobacterial infection of bone marrow macrophages. *Microbiology (Reading)* **148**:1991–1998. doi:10.1099/00221287-148-7-1991

Jo S, Kim T, Im W. 2007. Automated Builder and Database of Protein/Membrane Complexes for Molecular Dynamics Simulations. *PLOS ONE* **2**:e880. doi:10.1371/journal.pone.0000880

Jo S, Lim JB, Klauda JB, Im W. 2009. CHARMM-GUI Membrane Builder for Mixed Bilayers and Its Application to Yeast Membranes. *Biophysical Journal* **97**:50–58. doi:10.1016/j.bpj.2009.04.013

Jorgensen WL, Chandrasekhar J, Madura JD, Impey RW, Klein ML. 1983. Comparison of simple potential functions for simulating liquid water. *The Journal of Chemical Physics* **79**:926–935. doi:10.1063/1.445869

Kalscheuer R, Koliwer-Brandl H. 2014. Genetics of Mycobacterial Trehalose Metabolism. *Microbiology Spectrum* 10.1128/microbiolspec.mgm2-0002–2013. doi:10.1128/microbiolspec.mgm2-0002-2013

Kawaguchi K, Nagao H, Shindou H, Noguchi H. 2022. Conformations of Three Types of Ultra-Long-Chain Fatty Acids in Multicomponent Lipid Bilayers. *J Phys Chem B* **126**:9316–9324. doi:10.1021/acs.jpcb.2c06189

Khalid S, Schroeder C, Bond PJ, Duncan AL. 2022. What have molecular simulations contributed to understanding of Gram-negative bacterial cell envelopes? *Microbiology* **168**:001165. doi:10.1099/mic.0.001165

Klauda JB, Venable RM, Freites JA, O'Connor JW, Tobias DJ, Mondragon-Ramirez C, Vorobyov I, MacKerell ADJr, Pastor RW. 2010. Update of the CHARMM All-Atom Additive Force Field for Lipids: Validation on Six Lipid Types. *J Phys Chem B* **114**:7830–7843. doi:10.1021/jp101759q

Kumar Y, Basu S, Chatterji D, Ghosh A, Jayaraman N, Maiti PK. 2025. Self-Assembly of Mycolic Acid in Water: Monolayer or Bilayer. *Langmuir* **41**:3140–3156. doi:10.1021/acs.langmuir.4c03743

Lerner TR, Queval CJ, Fearns A, Repnik U, Griffiths G, Gutierrez MG. 2018. Phthiocerol dimycocerosates promote access to the cytosol and intracellular burden of Mycobacterium tuberculosis in lymphatic endothelial cells. *BMC Biology* **16**:1. doi:10.1186/s12915-017-0471-6

Marrakchi H, Lanéelle M-A, Daffé M. 2014. Mycolic Acids: Structures, Biosynthesis, and Beyond. *Chemistry & Biology* **21**:67–85. doi:10.1016/j.chembiol.2013.11.011

Mishra AK, Driessen NN, Appelmelk BJ, Besra GS. 2011. Lipoarabinomannan and related glycoconjugates: structure, biogenesis and role in Mycobacterium tuberculosis physiology and host–pathogen interaction. *FEMS Microbiology Reviews* **35**:1126–1157. doi:10.1111/j.1574-6976.2011.00276.x

Modak B, Girkar S, Narayan R, Kapoor S. 2022. Mycobacterial Membranes as Actionable Targets for Lipid-Centric Therapy in Tuberculosis. *J Med Chem* **65**:3046–3065. doi:10.1021/acs.jmedchem.1c01870

Mulholland CV, Wiggins TJ, Cui J, Vilchèze C, Rajagopalan S, Shultis MW, Reyes-Fernández EZ, Jacobs WR, Berney M. 2023. The PDIM paradox of Mycobacterium tuberculosis: new solutions to a persistent problem. *bioRxiv* 2023.10.16.562559. doi:10.1101/2023.10.16.562559

Nikaido H. 2003. Molecular Basis of Bacterial Outer Membrane Permeability Revisited. *Microbiology and Molecular Biology Reviews* **67**:593–656. doi:10.1128/mmbr.67.4.593-656.2003

Park S, Im W, Pastor RW. 2021. Developing initial conditions for simulations of asymmetric membranes: a practical recommendation. *Biophysical Journal* **120**:5041–5059. doi:10.1016/j.bpj.2021.10.009

Poger D, Mark AE. 2015. A Ring to Rule Them All: The Effect of Cyclopropane Fatty Acids on the Fluidity of Lipid Bilayers. *J Phys Chem B* **119**:5487–5495. doi:10.1021/acs.jpcb.5b00958

Quigley J, Hughitt VK, Velikovsky CA, Mariuzza RA, El-Sayed NM, Briken V. 2017. The Cell Wall Lipid PDIM Contributes to Phagosomal Escape and Host Cell Exit of Mycobacterium tuberculosis. *mBio* **8**:e00148-17. doi:10.1128/mBio.00148-17

Rawicz W, Olbrich KC, McIntosh T, Needham D, Evans E. 2000. Effect of Chain Length and Unsaturation on Elasticity of Lipid Bilayers. *Biophysical Journal* **79**:328–339. doi:10.1016/S0006-3495(00)76295-3

Ryckaert J-P, Ciccotti G, Berendsen HJC. 1977. Numerical integration of the cartesian equations of motion of a system with constraints: molecular dynamics of *n*-alkanes. *Journal of Computational Physics* **23**:327–341. doi:10.1016/0021-9991(77)90098-5

Savintseva LA, Steshin IS, Avdoshin AA, Panteleev SV, Rozhkov AV, Shirokova EA, Livshits GD, Vasyankin AV, Radchenko EV, Ignatov SK, Palyulin VA. 2023. Conformational Dynamics and Stability of Bilayers Formed by Mycolic Acids from the Mycobacterium tuberculosis Outer Membrane. *Molecules* **28**:1347. doi:10.3390/molecules28031347

Silhavy TJ, Kahne D, Walker S. 2010. The Bacterial Cell Envelope. *Cold Spring Harb Perspect Biol* **2**:a000414. doi:10.1101/cshperspect.a000414

Steinbach PJ, Brooks BR. 1994. New spherical-cutoff methods for long-range forces in macromolecular simulation. *Journal of Computational Chemistry* **15**:667–683. doi:10.1002/jcc.540150702

Torrelles JB, Chatterjee D. 2023. Collected Thoughts on Mycobacterial Lipoarabinomannan, a Cell Envelope Lipoglycan. *Pathogens* **12**:1281. doi:10.3390/pathogens12111281

Vasyankin AV, Panteleev SV, Steshin IS, Shirokova EA, Rozhkov AV, Livshits GD, Radchenko EV, Ignatov SK, Palyulin VA. 2024. Temperature-Induced Restructuring of Mycolic Acid Bilayers Modeling the Mycobacterium tuberculosis Outer Membrane: A Molecular Dynamics Study. *Molecules* **29**:696. doi:10.3390/molecules29030696

Vermeer LS, de Groot BL, Réat V, Milon A, Czaplicki J. 2007. Acyl chain order parameter profiles in phospholipid bilayers: computation from molecular dynamics simulations and comparison with 2H NMR experiments. *Eur Biophys J* **36**:919–931. doi:10.1007/s00249-007-0192-9

Wu EL, Fleming PJ, Yeom MS, Widmalm G, Klauda JB, Fleming KG, Im W. 2014. *E. coli* Outer Membrane and Interactions with OmpLA. *Biophysical Journal* **106**:2493–2502. doi:10.1016/j.bpj.2014.04.024